Inorganic Chemistry

Article

pubs.acs.org/IC

Cobaloxime-Based Artificial Hydrogenases

Marine Bacchi,[†] Gustav Berggren,[†,‡] Jens Niklas,[§] Elias Veinberg,[¶] Michael W. Mara,[∥] Megan L. Shelby,[∥] Oleg G. Poluektov,[§] Lin X. Chen,[§,∥] David M. Tiede,[§] Christine Cavazza,[†] Martin J. Field,[¶] Marc Fontecave,[†,⊥] and Vincent Artero*[,†]

[†]Laboratory of Chemistry and Biology of Metals, Université Grenoble Alpes, CNRS, CEA, 17 rue des Martyrs, F-38000 Grenoble, France

[§]Chemical Sciences and Engineering Division, Argonne National Laboratory, 9700 South Cass Avenue, Lemont, Illinois 60439, United States

[¶]DYNAMO/DYNAMOP, Institut de Biologie Structurale, UMR CNRS/Université Grenoble Alpes/CEA 5075, EPN Campus, 6 rue Jules Horowitz F-38000 Grenoble, France

[∥]Department of Chemistry, Northwestern University, 2145 Sheridan Road, Evanston, Illinois 60208, United States

[⊥]Laboratoire de Chimie des Processus Biologiques, UMR 8229 (Collège de France, CNRS, Université Pierre et Marie Curie), 11 place Marcellin Berthelot 75005 Paris, France

Supporting Information

ABSTRACT: Cobaloximes are popular H_2 evolution molecular catalysts but have so far mainly been studied in nonaqueous conditions. We show here that they are also valuable for the design of artificial hydrogenases for application in neutral aqueous solutions and report on the preparation of two well-defined biohybrid species via the binding of two cobaloxime moieties, $\{Co(dmgH)_2\}$ and $\{Co(dmgBF_2)_2\}$ ($dmgH_2$ = dimethylglyoxime), to apo *Sperm-whale* myoglobin (*Sw*Mb). All spectroscopic data confirm that the cobaloxime moieties are inserted within the binding pocket of the *Sw*Mb protein and are coordinated to a histidine residue in the axial position of the cobalt complex, resulting in thermodynamically stable complexes. Quantum chemical/molecular mechanical docking calculations indicated a coordination preference for His93 over the other histidine residue (His64) present in the vicinity. Interestingly, the redox activity of the cobalt centers is retained in both biohybrids, which provides them with the catalytic activity for H_2 evolution in near-neutral aqueous conditions.

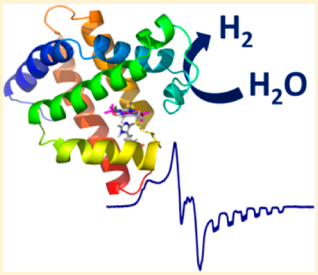

INTRODUCTION

Hydrogenases catalyze the reversible reduction of protons into molecular hydrogen. They function at thermodynamic equilibrium[1] and display very high turnover frequencies,[2] thereby making them competitive as unique efficient molecular catalysts with respect to platinum metal for H_2/H^+ interconversion.[3] Because their active sites contain only earth-abundant first-row transition metals, such as iron and nickel, a number of biomimetic[4−6] and bioinspired[7−10] synthetic catalysts for H_2 evolution have been reported over the last 2 decades. In particular, cobaloximes[11−14] (Figure 1) and diimine−dioxime cobalt complexes[15−18] have proved to be among the most active H_2-evolving catalysts in nonaqueous media.

Few studies have addressed the activity of this class of catalysts in fully aqueous conditions.[18−24] In general, it seems that molecular cobalt-based catalysts such as cobaloximes or diimine−dioxime cobalt complexes are not very active at pH 7, and we have recently shown that they get converted into cobalt-based nanoparticles during turnover in a phosphate aqueous buffer at pH 7.[25] A possible route to stabilization of these catalysts for applications in neutral aqueous media is through better control of the immediate environment of the active center. Inspiration has come recently from metalloproteins in the form of so-called artificial enzymes.[6,26−29] Indeed, in metalloenzymes, the polypeptidic framework controls the solvent accessibility and provides the active site with a surrounding of low permittivity and polarity, thus both tuning its catalytic activity and protecting it against undesired decomposition reactions.[30] Artificial enzymes, in which a molecular synthetic catalyst is embedded in a well-chosen peptide or protein, have recently proved to be catalytically active in water.[6,30] Interestingly, the hydrophobic self-assembly of $[Co(dmgH)_2(py)Cl]$ ($dmgH_2$ = dimethylglyoxime) with photosystem I yields a hybrid complex capable of photodriven H_2 production.[31]

These promising results led us to construct artificial hydrogenases based on cobaloximes, namely, the difluoroboryl-annulated cobaloxime $[Co(dmgBF_2)_2(H_2O)_2]$ (**1**; Figure 1) and the proton-bridged cobaloxime $[Co(dmgH)_2(H_2O)_2]$ (**2**, Figure 1). *Sperm-whale* myoglobin (*Sw*Mb; Figure 1) was chosen as the host protein because of its capability to bind several square-planar complexes[32−36] (including its natural

Received: May 9, 2014
Published: July 16, 2014

   dx.doi.org/10.1021/ic501014c | *Inorg. Chem.* 2014, 53, 8071−8082

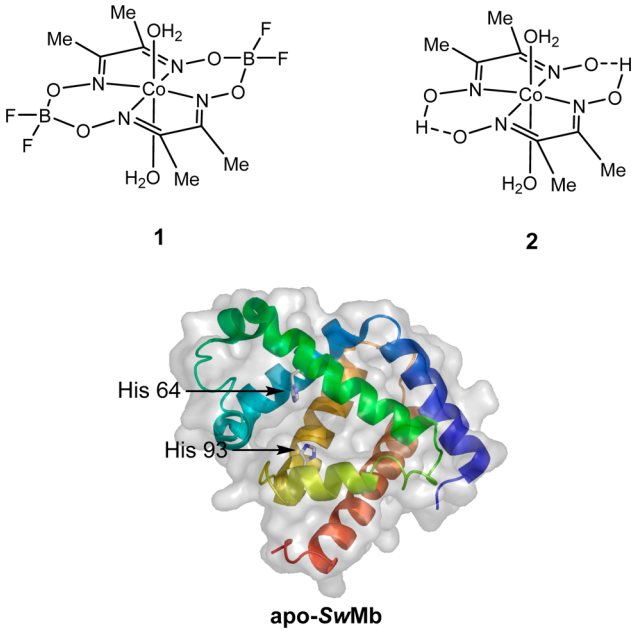

Figure 1. Molecular structure of the cobaloximes **1** and **2** and representation of apo-*Sw*Mb (PDB code 1UPD) showing both histidine residues present in its binding pocket.

cofactor, hemin) through coordination, in the axial position, of the metal ion to a histidine residue (His93) appropriately located in its hydrophobic cavity.[32,33,37] We report here on the preparation as well as the biochemical and spectroscopic characterization of two cobaloxime–*Sw*Mb biohybrids, *Sw*Mb·**1** and *Sw*Mb·**2**, capable of catalytic H_2 evolution.

EXPERIMENTAL SECTION

Materials. Hemin, $EuCl_2$, (ethylene glycol)bis(2-aminoethyl ether)-*N*,*N*,*N*′,*N*′-tetraacetic acid (EGTA), and Nafion solution (5% in ethanol) were purchased from Sigma-Aldrich. $[Co(dmgH)_2(H_2O)_2]$ (**2**),[38] $[Co(dmgBF_2)_2(H_2O)_2]$ (**1**),[39] $[Ru(bipy)_3]Cl_2$,[40] and 5-deazaflavin (DAF)[41] were prepared according to reported procedures. Commercial-grade C100 multiwalled carbon nanotubes (MWCNTs; >95%) were obtained from Nanocyl. *S*-(2,2,5,5-tetramethyl-2,5-dihydro-1*H*-pyrrol-3-yl)methylmethanesulfonothioate (MTSL) was purchased from Reanal Private Ltd. (Budapest, Hungary).

The production in *Escherichia coli* and purification of recombinant *Sperm-whale* myoglobin (*Sw*Mb) were performed according to a reported procedure with some modifications.[42] In this procedure, apo-*Sw*Mb was obtained from resolubilization of inclusion bodies in 0.1% trifluoroacetic acid aqueous solutions followed by two successive dialyses against 20 mmol L^{-1} Tris-acetate (pH 5.0) and 50 mmol L^{-1} Tris-HCl (pH 7.5) solutions (precipitated proteins were eliminated through centrifugation at each step). Further purification was performed through gel filtration (size-exclusion chromatography) using a Superdex 75 Hiload 16/60 Prepgrade column equilibrated with 50 mmol L^{-1} Tris-HCl (pH 8.0) and 20 mmol L^{-1} NaCl buffer. UV–visible-monitored titration confirmed that the purified protein was fully reconstituted with 1 equiv of hemin.

Physical Measurements. UV–visible spectra were recorded with a Shimadzu UV-1800 spectrophotometer in quartz or plastic cells (1 cm optical pathway). Circular dichroism (CD) measurements were done using a Jasco J-810 spectrometer. Inductively coupled plasma mass spectrometry (ICP-MS) cobalt titration was performed at the Department of Biochemistry, Toxicology and Pharmacology of the Centre Hospitalier Universitaire de Grenoble. Inductively coupled plasma atomic emission spectrometry (ICP-AES) cobalt titration was performed at the Argonne National Laboratory on a Thermo Scientific iCAP 600 spectrometer with errors within 5%. Protein concentrations were determined through titration with Rose Bengal (using bovin serum albumin as a standard).[43]

Continuous-wave (CW) X-band (9 GHz) electron paramagnetic resonance (EPR) experiments were obtained with two distinct instruments: (i) a Bruker EMX spectrometer equipped with an Oxford ESR 910 cryostat for low-temperature studies (the microwave frequency was measured with a frequency counter and the magnetic field with an NMR gaussmeter); (ii) a Bruker ELEXSYS E580 EPR spectrometer (Bruker Biospin, Rheinstetten, Germany), equipped with a TE_{102} rectangular EPR resonator (Bruker ER 4102st) and a helium gas-flow cryostat (Air Product, Allentown, PA). The temperature was controlled by a Lakeshore cryogenic temperature controller (Westerville, OH) and was about 5 or 80 K. The field modulation used in the CW experiments led to a derivative-type line shape. High-frequency EPR measurements were performed at Argonne National Laboratory on a home-built D-band (130 GHz) spectrometer equipped with a single-mode TE_{011} cylindrical cavity.[44] High-frequency EPR spectra of the samples were recorded in pulse mode in order to remove the microwave phase distortion due to fast-passage effects. The absorption line shape of the EPR spectra was recorded by monitoring the electron spin-echo (ESE) intensity from a two-microwave-pulse sequence as a function of the magnetic field. The durations of the microwave pulses were 50 and 70 ns, and typical separation times between microwave pulses were 150–300 ns.

Data processing was done using Xepr (Bruker BioSpin) and the *Matlab 7.11.1* (MathWorks) environment. The magnetic parameters were obtained from theoretical simulation of the EPR spectra. The simulations were performed using the *EasySpin* software package (version 4.0.0).[45] The accuracy in the determination of the electronic **g** tensor for the set of multifrequency EPR spectra was estimated to be ±0.001 (relative). Note that the absolute error, depending on the calibration of the magnetic field at the sample position, is larger.

Biohybrid solutions for EPR measurements were prepared in 50 mmol L^{-1} Tris-HCl (pH 7.0), added with 100 mmol L^{-1} NaCl and 10% glycerol, and introduced into the glovebox in 4-mm-o.d. quartz tubes. Spin quantification was performed by a comparison of the integral intensities from spectra recorded under nonsaturating conditions with those from spectra of solutions of the MTSL spin label also recorded under nonsaturating conditions.

Co K-edge (7.709 keV) X-ray absorption near-edge structure (XANES) and extended X-ray absorption fine structure (EXAFS) spectra were collected at the Beamline 12BM at the Advanced Photon Source of Argonne National Laboratory. Si(111) doublet crystals were used in the monochromator. A platinum-coated mirror was used to focus the beam and to remove higher harmonic X-ray photons. The beam size at the sample was approximately 0.4 mm (v) × 1 mm (h). A feedback system was used to control the monochromator crystal angle and was set to 70% detuning. A 13-element germanium solid-state detector (Canberra) was used to collect iron X-ray fluorescence signals. An iron filter was placed in front of the detector for attenuation of elastic scatterings, which increased the signal ratio between the fluorescence and elastic scattering of the sample from <1:100 to ∼1:1. The outputs from the amplifiers of the detector were connected to an array of single-channel analyzers (SCAs) with upper and lower thresholds set to allow only $K\alpha_1$ and $K\alpha_2$ fluorescence signals to be further processed. An ion chamber was placed before the sample for the incident X-ray flux reference signal I_0, and the second and third ion chambers were placed after the sample. A cobalt foil inserted between the second and third ion chambers was used for energy calibration. The output signals from the SCAs were connected to a scalar array, which interfaced with a computer hosting a data acquisition program (G. Jennings, Argonne National Laboratory). A Tris-HCl buffer and glycerol (10%) mixture was used to prevent ice crystal formation for the X-ray absorption spectroscopy measurements at 20 K. Complex **1** was measured in an acetonitrile solution, and the sample solution was studied inside a cryostat (Janis model CCS-150) at 20 K.

All electrochemical measurements were carried out under nitrogen at room temperature. A standard three-electrode configuration was used consisting of a CNT-based working electrode (see below), an auxiliary platinum wire, and an Ag/AgCl/aqueous $AgCl_{sat}$ + 3 mol L^{-1}

dx.doi.org/10.1021/ic501014c | Inorg. Chem. 2014, 53, 8071–8082

KCl (denoted as Ag/AgCl throughout this text) reference electrode closed by a Vycor frit and dipped directly into the solution. The $[Fe(CN)_6]^{3-}/[Fe(CN)_6]^{4-}$ couple (E^0 = 0.215 V vs Ag/AgCl or 0.425 V vs SHE in phosphate buffer at pH 7) was then used for standardization of the measurements in an aqueous solution.[46] The Fc^+/Fc couple (E^0 = 0.45 V vs Ag/AgCl) was used as a reference when a 0.1 mol L^{-1} nBu_4NBF_4/CH_3CN solution was used as the electrolyte. Cyclic voltammograms were recorded with a Biologic SP300 potentiostat. H_2 evolution was quantified with a micro-Clark H_2-MR sensor connected to a microsensor monometer from Unisense, calibrated with 100%, 40%, and 10% H_2-saturated deionized water. Irradiation was performed with a 300 W xenon lamp (Oriel, ozone free) operated at 280 W coupled with a water-filled Spectra-Physics 6123NS liquid filter for elimination of IR radiation and, for the experiments using a ruthenium-based photosensitizer, a Spectra-Physics 59472 UV cutoff filter (λ > 400 nm).

Theoretical Calculations. Calculations of the isolated cobalt complexes were done with a quantum-chemical (QC) density functional theory (DFT) approach using the B3LYP functional[47−49] and a triple-ζ def2-TZVP basis set.[50] The *ORCA* program package was employed for all electronic structure calculations.[51] All geometry optimizations were performed with an implicit solvent model appropriate to acetonitrile using the *COSMO* method.[52,53]

Docking calculations were carried out with a mixture of molecular mechanical (MM) and hybrid QC/MM potentials using the *pDynamo* modeling program.[54] Starting structures for the proteins were taken from the protein data bank (*Sw*Mb PDB code 1UPD) with all nonprotein groups removed and protonation states for the appropriate residues assigned using *ProPKA*.[55] The structures of the cobalt complexes were obtained from the previously performed DFT calculations. The initial structures for the docking were obtained by placing the cobalt complexes in the sites vacated by the protein prosthetic group with a $Co-N_{His}$ distance of 2.5 Å. These initial structures were then energy-minimized using a mixture of geometry optimization and molecular dynamics simulation with the OPLS-AA MM force field.[56] The atoms of all residues within 5 Å of the complex were left free to move in the simulations, whereas the atoms of protein residues further away than this were harmonically restrained to their original positions. The $Co-N_{His}$ distance was harmonically constrained at 2.5 Å. Optimizations were performed at 10° increments of the complex about the $Co-N_{His}$ axis and the resulting structures ranked with respect to their energy. Similar calculations were performed for the cases in which water was coordinated to the cobalt distal to the histidine, with the $Co-O_{water}$ distance harmonically constrained at 1.9 Å. QC/MM calculations of the lowest-energy MM-optimized structures were then performed using the semiempirical PM6 method[57] and the same OPLS-AA force field as that above. The QC region contained the cobalt complex, the side chain of the coordinating histidine (the CH_2 imidazole group), and, if present, the water. Optimizations using this potential were carried out in the same way as the MM optimizations but without the harmonic constraints between the cobalt and coordinating histidine and water groups because these interactions are now treated at the QC level of theory.

Preparation of the Biohybrid *Sw*Mb·1. The biohybrid was prepared in a glovebox under a wet dinitrogen atmosphere at 18 °C. A solution of **1** (500 μL, 1 mmol L^{-1}) in 50 mmol L^{-1} Tris-HCl (pH 7.0) was slowly added to a solution of *Sw*Mb (500 μL, 1.7 mg mL^{-1} or 0.1 mmol L^{-1}). The yellow solution was stirred for 1 h at 4 °C, transferred to a NAP10 desalting column, and eluted with the same buffer. The yellow protein fraction was collected (1 mL, 0.76 mg mL^{-1} or 0.45 mmol L^{-1}; 90% yield) and kept under an inert atmosphere throughout the study, unless otherwise stated.

Preparation of the Biohybrid *Sw*Mb·2. The biohybrid was prepared in a glovebox under a wet dinitrogen atmosphere at 18 °C. A solution of **2** (500 μL, 1 mmol L^{-1}) in 50 mmol L^{-1} Tris-HCl (pH 7.0) was slowly added to a solution of *Sw*Mb (500 μL, 3.6 mg mL^{-1} or 0.2 mmol L^{-1}). The yellow solution was stirred for 1 h at 4 °C, transferred to a NAP10 desalting column, and eluted with the same buffer. The yellow protein fraction was collected (1 mL, 1.2 mg mL^{-1} or 0.7 mmol L^{-1}; 66% yield) and kept under an inert atmosphere throughout the study, unless otherwise stated.

Preparation of Modified CNT Electrodes. A suspension of MWCNTs (29 mg) in absolute ethanol (210 mL) was homogeneized through sonication. Aliquots of 10 μL were successively deposited onto a Teflon-embedded glassy carbon electrode (5 mm o.d.) until the electroactive surface was totally covered. The electrode was dried in air, and then a drop (15 μL) of the proteic solution was deposited onto the surface of the MWCNTs. A Nafion solution (15 μL) was eventually added after drying in air.

Catalytic Assays with Europium(II) Salts. The preparation was done in a glovebox under a wet dinitrogen atmosphere at 18 °C. A solution of $[Eu(EGTA)(H_2O)]^{2-}$ (200 mmol L^{-1}) in 1 mol L^{-1} Tris-HCl (pH 8.0) buffer was prepared from equivalent volumes of stock solutions (400 mmol L^{-1}) of $EuCl_2$ and EGTA. Solutions of biohybrids (*Sw*Mb·**1** or *Sw*Mb·**2**) were prepared in situ from a solution of *Sw*Mb (typically 100 μL, 0.1 mmol L^{-1}) in 50 mmol L^{-1} Tris-HCl (pH 7.0) buffer and a solution of **1** or **2** (10 μL, 0.8 mmol L^{-1}) in deionized water; **1** or **2** was purposely introduced slightly substoichiometrically to ensure complete binding to the protein. This solution was transferred into Unisense 400 μL MicroRespiration chambers, taken out of the glovebox, and the H_2 microsensor was plunged into the solution. Once the signal stabilized for 10 min, the europium(II) solution was added via a Hamilton syringe.

Photocatalytic Assays. The preparation was done in a glovebox under a wet dinitrogen atmosphere at 18 °C. Solutions of $[Ru(bipy)_3]Cl_2$ (10 mmol L^{-1}) and DAF (1.4 mmol L^{-1}; $\varepsilon_{400\ nm}$ = 12000 mol^{-1} L cm^{-1}) were prepared in deionized water. Solutions of biohybrids (*Sw*Mb·**1** or *Sw*Mb·**2**) were prepared in situ from a solution of *Sw*Mb (typically 100 μL, 0.1 mmol L^{-1}) in 50 mmol L^{-1} Tris-HCl (pH 7.0) buffer and a solution of **1** or **2** (10 μL, 0.8 mmol L^{-1}) in deionized water; **1** or **2** was purposely introduced slightly substoichiometrically to ensure complete binding to the protein.

In experiments based on $[Ru(bipy)_3]Cl_2$ as the photosensitizer, the biohybrid solution was diluted with 50 mmol L^{-1} potassium phosphate (pH 6) buffer complemented with NaCl (150 mmol L^{-1}) and sodium ascorbate (100 mmol L^{-1}). The solution was then transferred into Unisense 400 μL MicroRespiration chambers, taken out of the glovebox, and the H_2 microsensor was plunged into the solution. Once the signal stabilized for 10 min, the $[Ru(bipy)_3]Cl_2$ solution (20 equiv with regards to the cobalt catalyst) was added via a Hamilton syringe, and irradiation started.

In experiments based on DAF as the photosensitizer, the biohybrid solution was diluted with 50 mmol L^{-1} Tris-HCl (pH 7.0) buffer. The solution was then transferred into Unisense 400 μL MicroRespiration chambers, taken out of the glovebox, and the H_2 microsensor was plunged into the solution. Once the signal stabilized for 10 min, the DAF solution (0.5 equiv with regards to the cobalt catalyst) was added via a Hamilton syringe, and irradiation started.

RESULTS

Preparation and Biochemical Characterization of Biohybrids. Reaction of apo-*Sw*Mb [10−100 μmol L^{-1} in Tris-HCl buffer (pH 7.0)] with 5−10 mol equiv of the cobaloximes **1** and **2** yielded the biohybrids *Sw*Mb·**1** and *Sw*Mb·**2**, respectively. The excess of cobaloxime was removed using size-exclusion chromatography. Quantitative analysis of cobalt (ICP-MS or ICP-AES) and protein (Rose Bengal method) indicated the presence of one cobalt complex per polypeptide chain. Concentration through centrifugation on membranes with 3 kDa cutoff was limited because it generally resulted in a loss of the cobalt complex (approximately 30% and 60% for preparing solutions with 1 and 2 mmol L^{-1} final protein concentrations, respectively). Calibrated size-exclusion gel chromatography confirmed the monomeric nature of the biohybrids, which coelute with apo- and holo-*Sw*Mb proteins.

UV−Visible Spectroscopy. The UV−visible spectra of solutions of *Sw*Mb·**1** and *Sw*Mb·**2** are shown in Figures 2 and

dx.doi.org/10.1021/ic501014c | Inorg. Chem. 2014, 53, 8071−8082

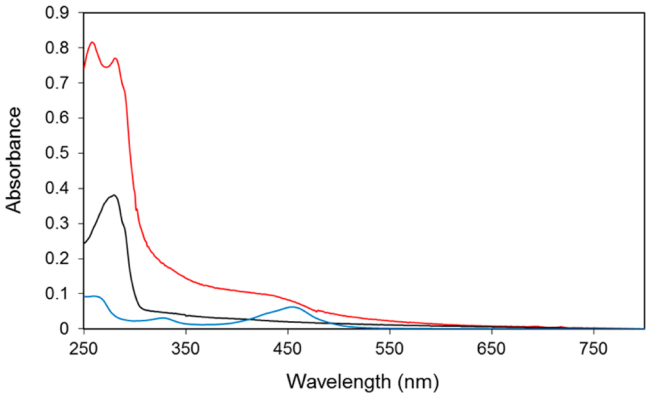

Figure 2. UV−visible spectra of 30 μmol L^{-1} solutions of apo-*Sw*Mb (black trace), **1** (blue trace), and *Sw*Mb·**1** (red trace) in 50 mmol L^{-1}Tris-HCl (pH 7.5).

S1 in the Supporting Information (SI), respectively, together with those of apo-*Sw*Mb and complexes **1** and **2** at the same concentration. The spectrum of *Sw*Mb·**1** shows features of the spectra of its two components: (i) a band in the 280 nm region characteristic of the protein; (ii) a band at 260 nm present in the spectrum of **1**; (iii) a broad and flat absorption band between 350 and 450 nm, related to the two absorption features of complex **1** (327 nm, ε = 1.7 × 10^3 mol^{-1} L cm^{-1}, and 455 nm, ε = 3 × 10^3 mol^{-1} L cm^{-1}) that are due to d−d transitions in the cobalt(II) center.[58] The blue shift and broadening of these bands are caused not only by the polypeptide environment but also by coordination of His93 because the histidine ligand is a stronger ligand than water. Figure S2 in the SI underlines that these bands are similarly affected when **1** is treated with increasing concentrations of imidazole. By contrast, the UV−visible spectrum of *Sw*Mb·**2** lacks the specific absorption band expected for a cobalt(II) center.[58] Instead, an important shoulder is observed in the 300−400 region in addition to the absorption band of the protein at 280 nm. This shoulder is reminiscent of the absorption of cobalt(III) cobaloximes such as [Co($gH)_2$pyCl] (gH_2 = glyoxime; Figure S1 in the SI).

We investigated the possibility of replacing **1** and **2** by hemin in *Sw*Mb·**1** and *Sw*Mb·**2**, a strategy previously used by Watanabe and co-workers to assess the presence of Schiff-base complexes within the *Sw*Mb cavity.[33] When apo-*Sw*Mb (10 μmol L^{-1}) was treated with 1 equiv of hemin at room temperature, holo-*Sw*Mb formed within a few minutes. Conversely, no hemin could be incorporated into *Sw*Mb·**1** or *Sw*Mb·**2** under the same conditions, as shown by UV−visible spectroscopy (Figures 3 and S3 in the SI). This observation further supports the hypothesis that the cobaloximes occupy the hemin binding site.

CD. Figure 4 compares the CD spectrum of *Sw*Mb·**2** in the UV region with those of apo- and holo-*Sw*Mb. Similar data were obtained with *Sw*Mb·**1**. The spectra all show features at 205 and 225 nm associated with the presence of α-helices. The signal in the 190−200 nm region in the holo-*Sw*Mb spectrum, absent in that of apo-*Sw*Mb, has been assigned to a specific local protein folding around the heme through coordination by His93.[59,60] The same signal is observed in the spectra of both biohybrids, further supporting the hypothesis that the cobalt complexes are coordinated by His93 in the biohybrids.

EPR Spectroscopy. The EPR spectrum of a *Sw*Mb·**1** solution shown in Figure 5 is typical for low-spin (S = $^1/_2$)

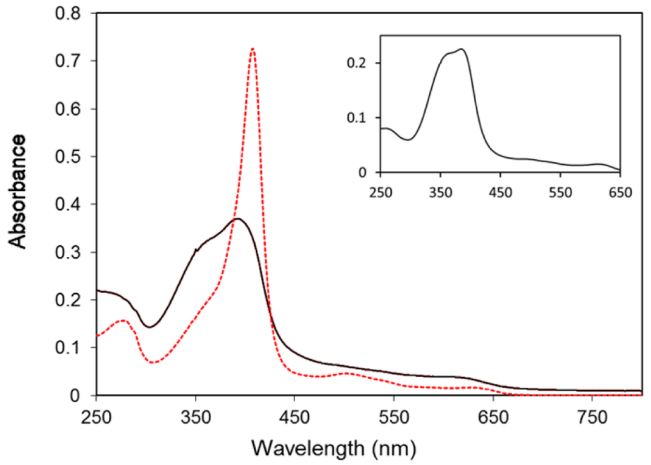

Figure 3. UV−visible spectra of 10 μmol L^{-1} solutions [50 mmol L^{-1} Tris-HCl (pH 7.5)] of *Sw*Mb·**1** reacted for 4 h with 1 equiv of hemin (black trace) and holo-*Sw*Mb (red dotted trace). The spectrum of free hemin (10 μmol L^{-1}) under similar conditions is shown in the inset.

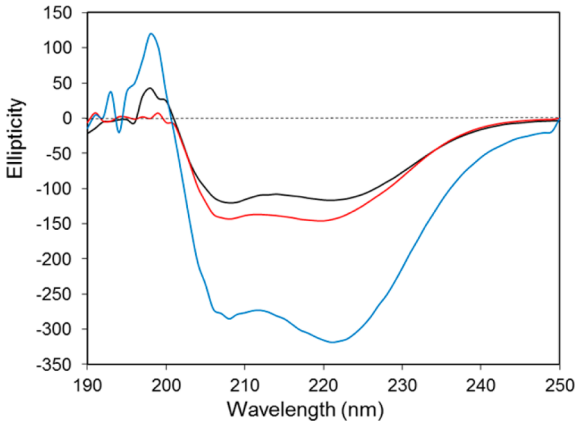

Figure 4. CD spectra of 80 μmol L^{-1} solutions of *Sw*Mb·**2** (black trace), apo-*Sw*Mb (red trace), and holo-*Sw*Mb (blue trace).

cobalt(II) in cobaloximes.[61,62] A basic analysis can be performed using the high-field part of the spectrum. The hyperfine coupling with the ^{59}Co nucleus (I = $^7/_2$; 100% natural abundance) results in the splitting of the g_z component into eight signals, six of which are easily distinguishable in the high-field region. Each of these signals exhibits a three-line pattern (1.4 mT splitting) that indicates axial coordination by a single nitrogen atom (I = 1; >99% natural abundance), likely from a histidine residue. Extensive previous EPR studies of this and closely related cobaloximes in a variety of solvents have shown that cobaloximes without an axial nitrogen atom or with two axial coordinating nitrogen atoms look entirely different.[61−64] As an example, Figure 5 shows a spectrum of **1** in methanol, where no axial coordination by nitrogen takes place. Unbound cobaloxime in an aqueous solution (Table 1) gives an EPR spectrum very similar to the one obtained in methanol.[61]

Spin quantification determined the cobalt(II) low-spin cobaloxime mole fraction to only account for approximately 36% of the cobalt concentration in the sample. For comparison, spin quantification on samples of **1** in methanol (Figure 5) is in agreement with 100% of the metal content being low-spin cobalt(II). Broad-field sweeps were performed at X band (Figure S4 in the SI), but no sign of high-spin cobalt(II) or other paramagnetic cobalt species[65,66] was detected. The pulsed

dx.doi.org/10.1021/ic501014c | Inorg. Chem. 2014, 53, 8071−8082

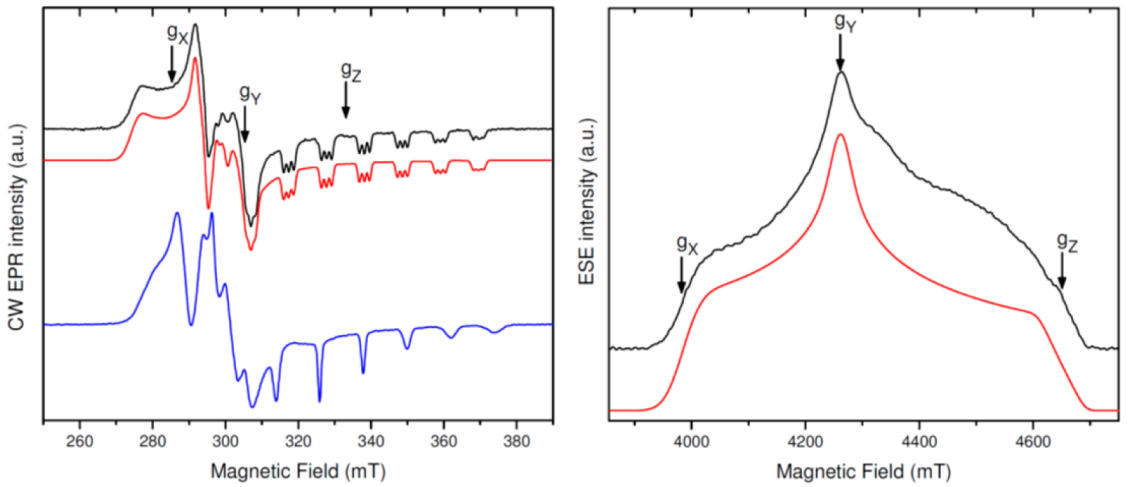

Figure 5. Left: Comparison of the experimental (black trace) and simulated (red trace) CW X-band EPR spectra (9.34 GHz) of a solution of *Sw*Mb·**1** (0.72 $mmol_{Co}$ L^{-1} and 1.8 $mmol_{SwMb}$ L^{-1}) in a frozen mixture of 50 mmol L^{-1} Tris-HCl (pH 7.0), 100 mmol L^{-1} NaCl, and 10% glycerol recorded at 5 K. The positions of the **g**-tensor principal components are shown by arrows. The spectrum of **1** in methanol (no axial coordination by nitrogen), shown in blue, is provided for easy comparison. Right: ESE-detected high-frequency (D-band, 130 GHz) EPR spectra of *Sw*Mb·**1**; T = 9 K; absorptive line shape. The positions of the **g**-tensor principal components are shown by arrows.

Table 1. EPR Simulation Parameters for the $\{Co(dmgBF_2)_2\}$ Moiety in Different Surroundings Including *Sw*Mb·1[a]

solvent/ligand(s)/ protein	g_x	g_y	g_z	$\|A\|(^{59}Co)$ [MHz]	$\|A\|(^{14}N)$ [MHz]
*Sw*Mb·**1**	2.3365	2.1835	2.0010	80, 10, 292[b]	30, 30, 39[b]
1 in a glycerol/H_2O mixture	2.2750	2.1785	2.0065	15, 15, 329[b]	n/a
1 in methanol	2.2840	2.1820	2.0080	53, 20, 338[b]	n/a
1 + 1 equiv of pyridine in methanol	2.2380	2.1530	2.0058	10, 10, 285[b]	33, 36, 43
1 + 1 equiv of p-PDI[c] in toluene	2.3473	2.1815	2.0000	85, 10, 306[b]	30, 30, 40[b]

[a]All parameters besides those for the SwMb·**1** biohybrid (first line) have been taken from previous work.[61] Note that the signs of the hyperfine coupling constants A_x, A_y, and A_z could not be determined by analysis of the EPR spectra. Thus, only the magnitude is given. The ^{14}N hyperfine coupling constants refer to the axial ligand. [b]In these cases, the hyperfine coupling constants A_x and A_y were estimated from the line width. [c]p-PDI = *N*-cyclohexyl-*N*′-4-pyridyl-1,7-dipyrrolidinyl-perylene-3,4:9,10-tetracarboxylic acid bisimide.

D-band EPR spectrum (Figure 5) showed that at least one other minor paramagnetic species was present in the sample, with a relative broad line shape, although the identity of this/these minor species is unclear. The most likely reason for the difference between spin quantification and cobalt titration is that a significant part of the cobalt species is diamagnetic, most probably in the cobalt(III) oxidation state, which is in agreement with the XANES data discussed below. The sample of the *Sw*Mb·**2** biohybrid was found to be EPR-silent, which likely reflects the presence of a cobalt(III) cobaloxime unit, in agreement with its electronic absorption spectra (Figure S1 in the SI). The EPR spectra recorded at X and D bands have been simulated (Figure 5), and the magnetic parameters, including principal g values and ^{59}Co and ^{14}N hyperfine values, are given in Table 1.

XANES Measurements. Figure 6 displays the XANES spectra at the Co K-edge for the two biohydrids *Sw*Mb·**1** and *Sw*Mb·**2** together with the spectra of **1** (recorded in an acetonitrile solution) and of electrochemically generated one-electron-oxidized $\mathbf{1}^+$ (Co^{III}) recorded in CH_3CN. A comparison of the latter two shows that a significant upward edge shift would take place when Co^{II} is oxidized to Co^{III}, as well as when the coordination number in the complex increases. This edge

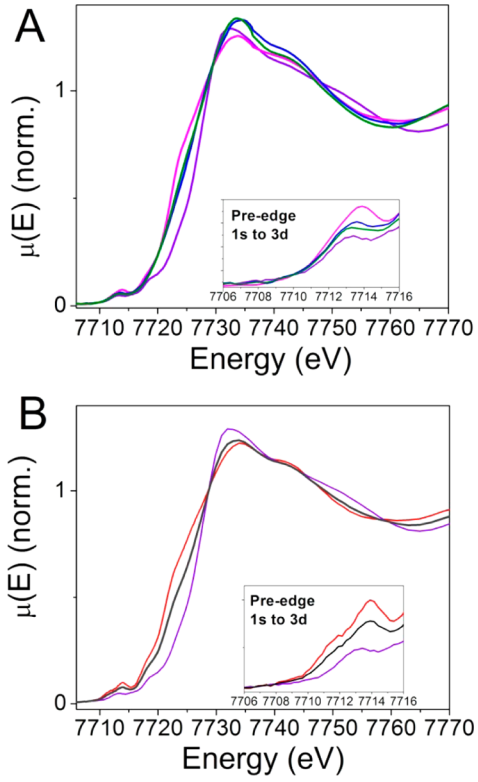

Figure 6. (A)Co K-near-edge spectra [$\mu(E)$, normalized absorption intensity vs photon energy] for *Sw*Mb·**1** (blue trace), *Sw*Mb·**2** (green trace), **1** (magenta trace, in acetonitrile), and electrochemically generated $\mathbf{1}^+$ (purple trace) at 20 K and (B) room-temperature spectra of CH_3CN solutions of **1** in the Co^{II} (red trace) and Co^{III} (purple trace) states generated via electrolysis along with the simulated spectrum with an approximately 1:1 ratio of the two corresponding spectra (black trace).

dx.doi.org/10.1021/ic501014c | *Inorg. Chem.* 2014, 53, 8071−8082

energy blue shift is visible from the spectra of *Sw*Mb·**1** and *Sw*Mb·**2** compared to the spectrum of **1**. However, the edge energies in the XANES spectra of *Sw*Mb·**1** and *Sw*Mb·**2** are still about 1 eV lower than that of $\mathbf{1}^{+}$ (Co^{III}). The spectrum simulated with a mixture of Co^{II} (50 ± 10%) and Co^{III} (50 ± 10%) species reproduces the features observed in *Sw*Mb·**1**. This result is in agreement with the EPR data, suggesting that an approximately 1:1 mixture of Co^{II} and Co^{III} is present in the biohybrid samples.

Meanwhile, the insets of Figure 6 focusing at the preedge region clearly show a higher intensity of the quadrupole-allowed 1s → $3d_{x^2-y^2}$ transition in the case of the cobalt(II) complex with respect to the cobalt(III) complex. The former has two preedge features, while the latter has only one weak feature (Figure 6B). On the basis of the nature of the quadrupole-allowed transition(s), it can be deduced that (i) cobalt(III) is most likely a low-spin species with only one (or one set of) vacant 3d orbital(s) and a nearly symmetric octahedral geometry and (ii) the cobalt(II) coordination geometry is less symmetric with a high-spin state, showing at least two vacant 3d orbital energy levels. The intensity of the preedge region is lower for the two biohybrids than for **1** (insets in Figure 6A,B), indicating that the coordination sphere is more symmetrical in the biohybrids. However, there is no sign of the second preedge feature in the low-temperature data of **1**, indicating that **1** ($3d^7$) has a low-spin state at 20 K with only one set of vacant and nearly isoenergetic 3d orbitals. Such a temperature-dependent spin-state formation has been commonly observed in iron species.[67] The higher preedge intensity also indicates some 3d−4p mixing[67] in **1**, but such a mixing is reduced in the biohybrids, which could be due to the fact that both cobalt(II) and cobalt(III) species gain a more symmetrical coordination sphere, most likely an octahedral geometry, when bound to the protein matrix.

Structural Studies. *EXAFS.* Figure 7 shows the EXAFS and Fourier-transformed EXAFS spectra of the two biohydrids *Sw*Mb·**1** and *Sw*Mb·**2** together with the spectrum of **1**.[68] The amplitude of the oscillations shown in Figure 7 (top) indicates a possible increase of the number of nearest-neighboring atoms ligated to the cobalt center and/or more uniform nearest-neighbor distances in the biohybrid samples compared to **1**. With the exception of this possible increase in the cobalt coordination number, no major structural changes are observed upon insertion of **1** into *Sw*Mb in terms of distances between the cobalt center and the first coordinating atoms. The same information can be drawn from the Fourier-transformed spectrum of **1** (Figure 7 (bottom)), in which the highest peak corresponds to the nearest Co−N or Co−O distances, i.e., the four equatorial as well as one or two axial ligands. In the *Sw*Mb·**1** and *Sw*Mb·**2** spectra, the intensity of this peak is significantly higher than that in the spectrum of **1**, indicating an increase of the coordination number (assigned to His93, see below) and/or a better uniformity in the bond distances between the cobalt center and the equatorial and axial ligands.

Docking. Docking calculations were initially performed with an MM energy function to identify the possible accommodation of the $\{Co(dmgBF_2)_2\}$ and $\{Co(dmgH)_2\}$ moieties within the *Sw*Mb cavity. Coordination of His93 to the cobalt center of both moieties was clearly more stable than coordination to the other histidine (His64) residues present in the cavity. From this model, an axial water molecule was coordinated in the trans position to His93 and the system was optimized using a QC/MM potential, with the QC region containing the cobalt

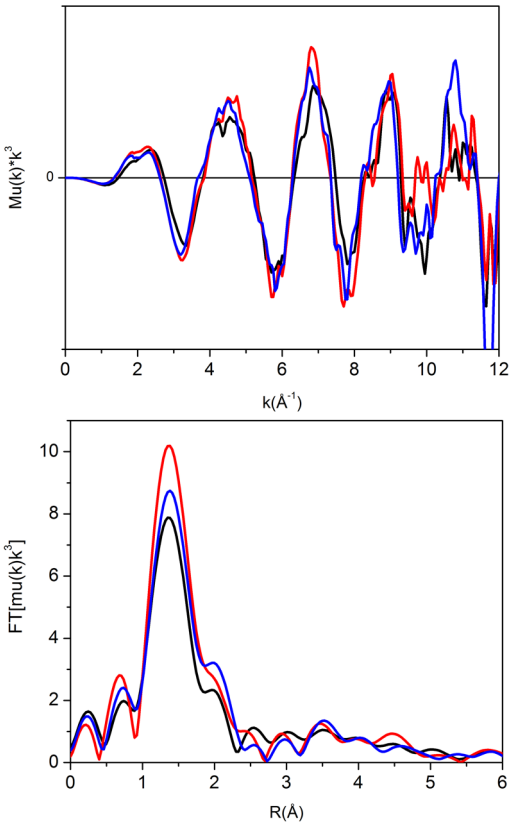

Figure 7. (Top) EXAFS spectra. (Bottom) Fourier-transformed EXAFS spectra of **1** (black trace), *Sw*Mb·**1** (red trace), and *Sw*Mb·**2** (blue trace).

complex and the side chain of the coordinating histidine. Figure 8 displays a superposition of the optimized structures around the metallic centers in both biohybrids. Other representations of these structures are shown in Figures 9 and S5 in the SI. At this level of theory, no dissociation of the axial ligands (either water or His93) was observed. In the case of *Sw*Mb·**2**, a hydrogen bond was established between the coordinated water molecule and His64 (with a $N^{\varepsilon}\cdots H$ distance of 2.02 Å). Such an interaction was not formed in the case of *Sw*Mb·**1** due to the displacement of His64 out of hydrogen-bonding range by the larger complex **1** ligand. Table 2 collects optimized structural data for both biohybrids and compares them to literature values for the structurally characterized $[Co(dpgBF_2)_2(CH_3CN)_2]$[13] and $[Co(dmgH)_2pyI]$[69] complexes. These data fit perfectly with the conclusions drawn from the EXAFS experiments.

Electrochemical Characterization. Cyclic voltammograms of the two biohybrids were recorded thanks to the fabrication of modified electrodes based on MWCNTs on which the biohybrids were adsorbed.[70,71] Coating of the resulting electrodes with Nafion significantly increased the stability of the resulting electrodes, which otherwise immediately released the biohybrid into the electrolyte solution. The cyclic voltammogram of *Sw*Mb·**1** immobilized on MWCNTs recorded in Tris-HCl (pH 7.5) buffer (Figure 10) displayed a reversible system at −0.48 V vs SHE, which can be assigned to the cobalt(II)/cobalt(I) couple of complex **1** accommodated in *Sw*Mb. The cyclic voltammogram of a millimolar solution of **1** recorded on the same MWCNT electrode (Figure 10) displays a reversible signal at −0.38 V vs SHE; i.e., the cobalt(II)/cobalt(I) couple in *Sw*Mb·**1** is located 100 mV more negative

dx.doi.org/10.1021/ic501014c | *Inorg. Chem.* 2014, 53, 8071−8082

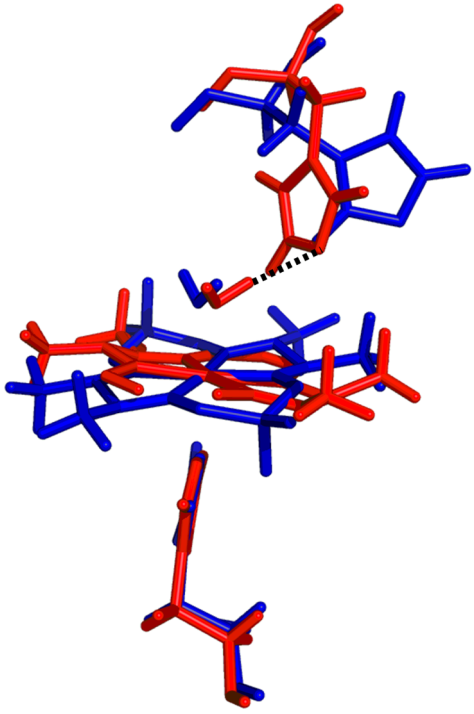

Figure 8. Superposition of the structures around the metallic centers in *Sw*Mb·**1** (blue) and *Sw*Mb·**2** (red) computed at the QC/MM level. From the polypeptide chains, only His93 (bottom) and His64 (top) are represented. The hydrogen bond between the cobalt-coordinated water molecule and His64 is shown in dashed-black in the case of *Sw*Mb·**2**.

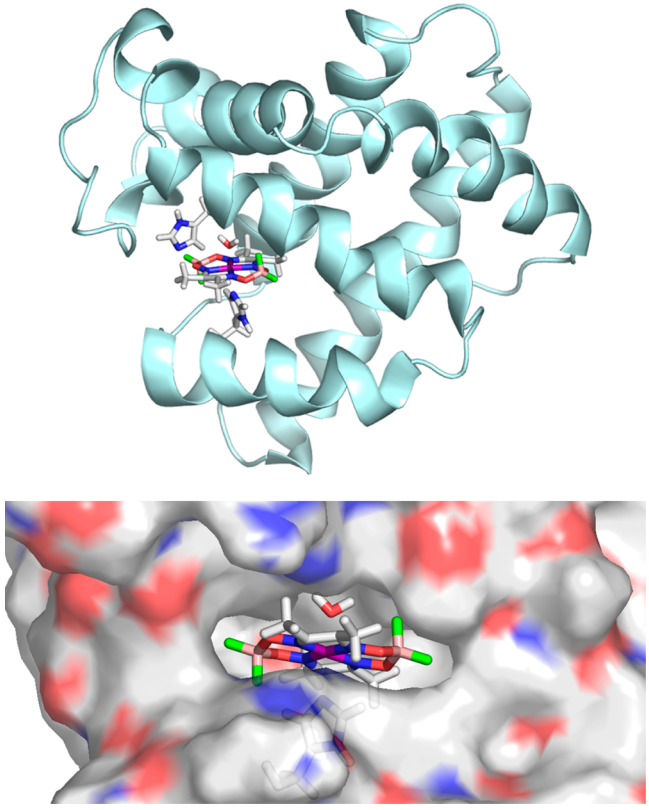

Figure 9. (Top) Structure of *Sw*Mb·**1** as computed at the QC/MM level. (bottom) Electrostatic representation of the protein environment around **1** in *Sw*Mb·**1**. The hydrophilic regions are shown in red (oxygen atoms) and blue (nitrogen atoms), while the hydrophobic regions are shown in gray. The cobalt atom is depicted in purple, boron in pink, and fluorine in green.

than that for **1** alone.[72] By contrast, the addition of imidazole (10 equiv) to a solution of **1** shifts the redox potential of the cobalt(II)/cobalt(I) couple more positive, although to a lower extent (40 mV; Figure S6 in the SI). This indicates that the redox properties of **1** in *Sw*Mb·**1** are not only controlled by coordination of the His ligand but also modulated by second-coordination-sphere interactions or the specific dielectric constant experienced by the complex within the protein framework. A specific effect of His coordination may be seen in the disappearance of the cobalt(III)/cobalt(II) signal[73] in the cyclic voltammogram of *Sw*Mb·**1**, paralleling the modification observed when imidazole is added to an aqueous solution of **1** (Figure S6 in the SI). The cyclic voltammogram of *Sw*Mb·**2** is shown in Figure S7 in the SI. It displays an ill-defined and irreversible signal with onset at −0.38 V vs SHE tentatively assigned to the cobalt(III)/cobalt(II) couple of the {Co(dmgH)$_2$(H$_2$O)His} moiety by comparison with the cyclic voltammogram of [Co(dmgH)$_2$Cl(py)].[12] No signal for cobalt(II)/cobalt(I) could be identified because this is overlapped by a large, probably catalytic, wave with onset at −0.6 V vs SHE assigned to H_2 evolution.

Catalytic Activity. The capability of both biohybrids for catalytic H_2 evolution from aqueous solutions at pH 7.0 was first assessed using the europium(II) complex [Eu(EGTA)(H$_2$O)]$^{2-}$ (10 equiv, 0.1 mmol L^{-1}). The H_2 concentration in the solution was monitored with a Unisense micro-Clark electrode, as shown in Figure 11 for experiments carried out with *Sw*Mb·**2** and **2** as the catalysts. Data are collected in Table 3. Under these conditions, in the case of *Sw*Mb·**2**, the reductant was consumed in about 5 min, generating H_2 with a 65% yield, corresponding to 3.2 turnovers (TON). *Sw*Mb·**2** slightly outperformed **2**, as far as the total TON is concerned, even if a slower initial reaction rate was observed (Figure 11). H_2 evolution could be restarted, although with a lower efficiency, via the addition of europium(II). By comparison, *Sw*Mb·**1** only achieved 0.3 TON under the same conditions, which was significantly lower than that of **1** (2 TONs).

H_2 evolution (Table 3) was also studied under photocatalytic conditions at pH 7.0, using DAF as the photosensitizer, whose excited state can capture an electron and a proton from Tris-HCl buffer, thus generating the radical species DAFH$^{\bullet}$.[74−77] This radical dimerizes spontaneously, but the latter reaction is reversible under light irradiation, generating a steady-state concentration of the reductive DAFH$^{\bullet}$ that can then transfer an electron to the cobalt-based catalyst. Under these conditions (Table 3), the catalytic performances of the two biohybrids were very close to those obtained at the same pH when [Eu(EGTA)(H$_2$O)]$^{2-}$ was used as the reductant. Larger TONs (3.8 and 3 TONs for *Sw*Mb·**1** and *Sw*Mb·**2**, respectively; Table 3) were obtained for *Sw*Mb·**1** under photocatalytic conditions at pH 6 in a phosphate buffer, using [Ru(bipy)$_3$]$^{2+}$ as the photosensitizer and ascorbate as a sacrificial electron donor. Under these conditions, photocatalytic proton reduction likely commences with reductive quenching of photoexcited [Ru(bipy)$_3$]$^{2+}$ by ascorbate, generating [Ru^{II}(bipy)$_2$(bipy$^{\bullet-}$)]$^{+}$, a potent reductant (E^0 = −1.12 V vs SHE), with a lifetime of ∼500 ns under these conditions. Then electron transfer to the cobalt-based catalyst can proceed, in competition with charge recombination between [Ru(bipy)$_3$]$^{+}$ and oxidized ascorbate,

dx.doi.org/10.1021/ic501014c | *Inorg. Chem.* 2014, 53, 8071−8082

Table 2. First Neighboring Atom Bond Lengths from Simulations (Docking Data for *Sw*Mb·1 and *Sw*Mb·2 and DFT Calculations with the B3LYP Functional and the TZVP Basis Set in an Implicit Solvent Model of Acetonitrile for $[Co(dmgBF_2)_2(CH_3CN)]$ and Experimental (Co K-Edge EXAFS) or Cobaloxime X-ray Structures

	bond lengths (Å)			
compound	Co–N(His$_p$)	Co–L	Co–N$_{eq}$(ligand) (min/max)	method
1		2.17 (L = CH_3CN)	1.90/1.91	DFT
*Sw*Mb·**1**	1.97	2.19 (L = H_2O)	1.87/1.9	QC/MM
*Sw*Mb·**2**	1.93	2.23 (L = H_2O)	1.93/1.95	QC/MM
$[Co(dpgBF_2)_2(CH_3CN)_2]$		2.241(3) (L = CH_3CN)	1.882(3)/1.889(3)	X-ray[13]
$[Co(dmgH)_2pyI]$	1.982(4)	2.582(1) (L = I^-)	1.887(4)/1.900(4)	X-ray[69]

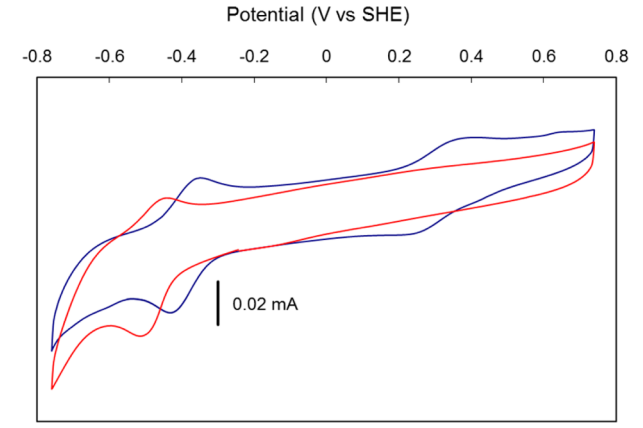

Figure 10. Cyclic voltammograms recorded in 100 mmol L^{-1} Tris-HCl (pH 7.5) buffer and 100 mmol L^{-1} NaCl of *Sw*Mb·**1** adsorbed on MWCNTs and coated with Nafion (red trace) and a solution of **1** (1 mmol L^{-1}, blue trace). Scan rate 100 mV s^{-1}.

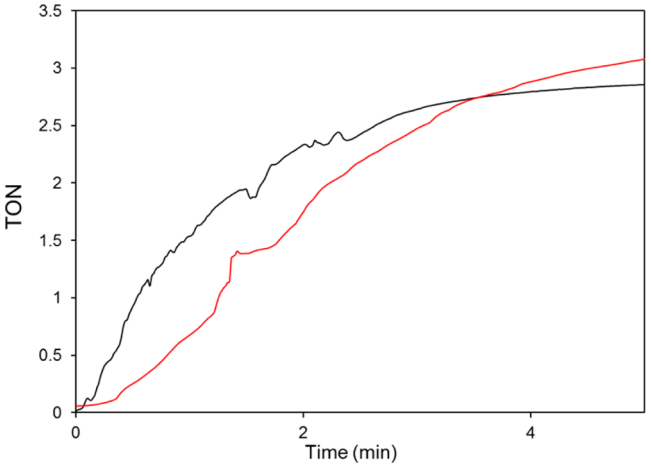

Figure 11. Catalytic H_2 evolution from a pH 7.0 aqueous solution of [Eu(EGTA)] (10 equiv with respect to the biohybrid in Tris-HCl buffer) in the presence of *Sw*Mb·**2** (red trace) and **2** (black trace). Both catalysts were at 10 μmol L^{-1} concentration. The H_2 concentration was monitored using a Unisense micro-Clark electrode.

both of which can be expected to occur at rates close to the diffusion limit. In all cases [thermal reduction by the europium(II) complex or photocatalytic conditions], the blue color of the cobalt(I) species[78] is observed immediately after the addition of the reducing agent, which supports the above mechanisms. It should be noted that confinement of the cobaloxime within the myoglobin cavity strongly constrains the mechanism of the H_2 evolution reaction, which may account for the lower activity observed for the biohybrids. Indeed, two

Table 3. Catalytic H_2 Evolution Mediated by *Sw*Mb·1, *Sw*Mb·2, 1, and 2 under Various Conditions[a]

	TON		
compound	[Eu(EGTA)(H_2O)]$^{2-}$ (pH 7)	hν/DAF/Tris (pH 7)	hν/[Ru(bipy)$_3$]$^{2+}$/ascorbate (pH 6)
1	2	2	5
2	2.5	8.3	7
*Sw*Mb·**1**	0.3	0.6	3.8
*Sw*Mb·**2**	3.2	5	3

[a]TONs are calculated versus the number of introduced cobalt centers.

mechanisms may occur in parallel for the free complex: in the first one, involving only one metal site, H_2 is produced via protonation of a metal-bound hydride ligand; the second one involves bimolecular H_2 elimination from two metal hydride molecules and is fully excluded in the case of the biohybrid species.[10]

DISCUSSION

*Sw*Mb has been used as a host protein for the construction of a variety of artificial enzymes that catalyze oxidation of organic substrates. Schiff-base complexes of chromium(III),[33,34] manganese(III),[34,35] iron(III),[32] and copper(II)[36] have been inserted within the cavity of the apo-*Sw*Mb host where they bind to a histidine residue. In most cases, His93, which is the natural ligand of hemin in holo-*Sw*Mb, coordinates the square-planar Schiff-base complexes in the axial position, as revealed by X-ray crystallography.[32] Cobaloximes possess square-planar geometry similar to Schiff-base complexes together with good affinity in their axial position for N-heterocyclic bases. Accordingly, the two cobaloximes **1** and **2** used in this study form pure, molecularly defined and stable biohybrids, *Sw*Mb·**1** and *Sw*Mb·**2**, upon reaction with apo-*Sw*Mb. All spectroscopic data confirm that the cobaloximes are inserted within the binding pocket of the folded *Sw*Mb protein and are coordinated to a histidine residue in the axial position of the cobalt complex, resulting in a very high association constant. QC/MM docking calculations indicated a coordination preference for His93 over the other histidine residue (His64) present in the vicinity. Structural data extracted from these calculations fit well with those obtained from EXAFS measurements on both biohybrids. In both cases, the cobalt center appears to be hexacoordinated with a water molecule, completing the coordination sphere of the cobaloxime complexes bound to the protein via axial His93. In the case of *Sw*Mb·**2**, the coordinated water molecule is hydrogen-bonded to His64.

The hydrophobic environment of the cobaloxime when inserted within the myoglobin cavity is demonstrated by a comparison of the *g* values extracted from EPR spectra of *Sw*Mb·**1** with those already reported for the $\{Co(dmgBF_2)_2\}$

dx.doi.org/10.1021/ic501014c | *Inorg. Chem.* 2014, 53, 8071–8082

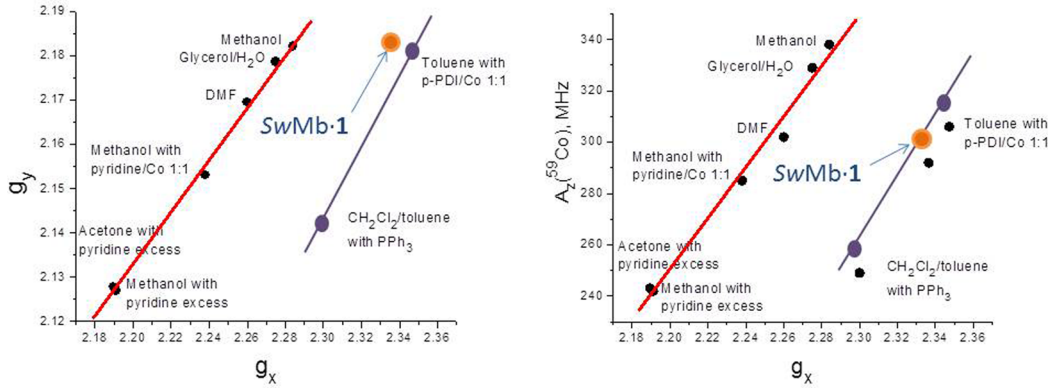

Figure 12. Correlation plots of g_y and $|A_z|(^{59}Co)$ vs g_x for the $\{Co(dmgBF_2)_2\}$ moiety in different solvents. All parameters besides those for the *Sw*Mb·**1** biohybrid have been taken from previous work.[61]

moiety in various compounds or media (Table 1). The graphical representations shown in Figure 12 indeed show two distinct correlation features between g_x and g_y on the one side and between g_x and A_z on the other side depending on the nature of the medium (protic and polar, red lines; aprotic and apolar, blue lines). The g values and hyperfine coupling constants with ^{59}Co and ^{14}N nuclei measured for *Sw*Mb·**1** are close to the blue lines in both representations. In particular, the observed values are very similar to the values measured in toluene, a very hydrophobic environment, for an adduct between $\{Co(dmgBF_2)_2\}$ and a pyridyl-modified perylene diimide (p-PDI).[79] p-PDI coordinates axially to the cobaloxime through a pyridine moiety, thus mimicking histidine coordination in the biohybrid. Such correlations will be highly valuable to characterize the immediate environment of the cobaloxime moieties in related protein systems such as the photosystem I based hybrid complex, for example.[31]

All of these data provide clear evidence that the cobaloxime is bound in the apo-myoglobin heme pocket and coordinated to only one of the two histidines available in the binding pocket. No other interactions with amino acid residues located in the pocket could be evidenced from the docking study, but we note that the cobaloxime ligands lack the propionate and ethyl residues that stabilize the heme cofactor in myoglobin through hydrogen bonds and hydrophobic interactions, respectively.

Electrochemical measurements on biohybrid-modified CNT electrodes demonstrated redox activity of the cobalt centers in both biohybrids. The potential of the cobalt(II)/cobalt(I) couple is significantly affected by the protein environment with a 100 mV negative shift. In the case of *Sw*Mb·**2**, the cyclic voltammogram recorded at pH 7 suggests catalytic activity for H_2 evolution with an onset potential at −0.6 vs SHE, thus corresponding to an overpotential requirement of ∼200 mV. Because the low stability of the biohybrid-modified CNT electrodes prevented detailed electrocatalytic studies, we turned to solution assays to assess the catalytic properties of the biohybrids. We used two different sets of conditions at pH 7.0 based either on thermal reduction of the catalyst by the europium(II) complex $[Eu(EGTA)(H_2O)]^{2-}$ reductant ($E^0_{Eu(II)/Eu(III)}$ = −0.88 vs SHE corresponding to $E_{Eu(II)/Eu(III)}$ = −0.64 to −0.70 vs SHE at the europium(II) concentrations used in this study;[80] the driving force for H_2 evolution is ∼220−280 mV) or light-driven reduction of the catalyst by a photogenerated DAFH$^\bullet$ radical (E^0 = −0.65 V vs SHE; the driving force for H_2 evolution is ∼240 mV). In both cases, the driving force for catalysis is thus only slightly higher than the overpotential requirement indicated by cyclic voltammetry measurements. Accordingly, *Sw*Mb·**2** displays catalytic activity both under thermal reduction by the europium(II) complex and in photocatalytic conditions.

By contrast, *Sw*Mb·**1** proved mostly inactive at pH 7. This decrease in activity in the biohybrid compared to that in complex **1** could be related to the 100 mV cathodic shift of the cobalt(II)/cobalt(I) process induced by the incorporation of the complex in the protein. Decreasing the pH value to 6 and using $[Ru(bipy)_3]^{2+}$ as the photosensitizer and ascorbate as a sacrificial electron donor allowed the observation of catalytic activity for *Sw*Mb·**1** (TON = 3.8). The requirement for acidic pH for catalytic H_2 evolution in the case of complex **1** was reported prior to this study. Connolly and Espenson initially reported efficient H_2 evolution activity for **1** using chromium(II), vanadium(II), or europium(II) salts as electron sources in a HCl solution (pH <1).[19] A further report from Szajna-Fuller and Bakac[20] using titanium(III) citrate as the electron source demonstrated that no activity could be observed at pH >4. Our results thus confirm the previous observation that only proton-bridged cobaloximes (related to complex **2**) can act as catalysts for H_2 evolution in neutral to basic conditions.[22,24,31] More acidic conditions (pH <5) would probably allow an increase in the H_2-evolving catalytic activity of *Sw*Mb·**1**. Unfortunately, myoglobin is not stable under such conditions where defolding occurs, and the cofactor is released into solution.

With an overpotential requirement in the 200 mV range, cobaloxime-based artificial hydrogenase thus proved competitive with cobalt porphyrin-based biohybrids, which require a much higher driving force (>800 mV) to catalyze H_2 evolution at pH 7.[81] They are unfortunately much less stable during turnover, probably because reduction of the dioxime ligands leads to their irreversible hydrogenation (and inactivation of the catalyst), while porphyrins can act as reversible electron reservoirs.

The two novel artificial hydrogenases *Sw*Mb·**1** and *Sw*Mb·**2**, however, compare well with other artificial enzymes based on dithiolate-bridged hexacarbonyldiiron catalytic units covalently attached to polypeptides[82−84] or incorporated within cytochrome *c*.[85,86] In these systems, larger polypeptides were found to enhance catalytic activities, pointing to the importance of the whole protein environment, as described in this study. Such biohybrid systems were shown to catalyze light-driven H_2 evolution in aqueous conditions and in the presence of $[Ru(bpy)_3]^{2+}$ as the photosensitizer and ascorbate as the sacrificial electron donor, resulting in total TONs of 5−9 (with

dx.doi.org/10.1021/ic501014c | *Inorg. Chem.* 2014, 53, 8071−8082

regard to the catalyst) at neutral to basic pH.[87] The reason for such a limited stability may be drawn from mechanistic considerations. In the case of cobaloxime-mediated H_2 evolution, the catalytic mechanism starts with protonation of a cobalt(I) species, yielding a Co^{III}-H species.[10] We note that a blue color assigned to a cobalt(I) or a Co^{III}-H species[78] is initially observed in the catalytic assays involving *Sw*Mb·**1** and *Sw*Mb·**2**. Reduction of this Co^{III}-H species is, however, required for catalysis to occur. Hydrogen is then heterolytically produced through rapid protonation of a Co^{II}-H species.[88−90] The limited stability observed upon turnover likely originates from deactivation of a catalytic intermediate such as the Co^{III}-H species. It has been proposed that hydride transfer from this latter species results in hydrogenation of the glyoximato ligand with the loss of catalytic activity.[91] Thus, a higher activity and stability would be expected if the delay between the two successive electron-transfer processes could be limited. Such fast electron injection is likely to occur in the photosystem I/cobaloxime biohybrid system and explains its exceptional stability.[31] Similar supramolecular control of the electronic communication between the photosensitizer and catalytic unit within artificial enzymes had been proven to be beneficial in the cases of dithiolate-bridged hexacarbonyldiiron catalytic units[86] and nickel bisdiphosphine complexes.[92]

■ CONCLUSION

A number of metallocenters have been incorporated into *Sw*Mb (and other heme proteins) to create functional catalysts.[30] Surprisingly, this strategy has only been applied to oxidation catalysts and never been used to prepare artificial hydrogenases.[6,29] We show here that cobaloxime can be easily installed in myoglobin through coordination to only one of the two histidines available in the binding pocket. The resulting biohydrids display catalytic activity for H_2 evolution under aqueous conditions and with low overpotential requirement (∼200 mV), which is key for further biotechnological application because this parameter directly impacts the energetic efficiency of electrochemical devices. The operational stability, another crucial requirement for technological implementation, appears to be limited to a few turnovers, as observed for most artificial hydrogenases described so far. This can be improved through enhanced electron communication with the electron donor as discussed above or active site engineering. The latter has previously been achieved for other artificial metalloenzymes,[28,93,94] some based on the myoglobin scaffold,[32,33,95] either through point mutation or exploration of the diversity of hemoproteins that could bind these and other synthetic cobalt catalysts.

■ ASSOCIATED CONTENT

Ⓢ Supporting Information

Full experimental details and additional Figures S1−S7 containing UV−visible and EPR spectra, electrochemical data, and a representation of calculated structures. This material is available free of charge via the Internet at http://pubs.acs.org.

■ AUTHOR INFORMATION

Corresponding Author

*E-mail vincent.artero@cea.fr. Tel: +33438789106.

Present Address

‡G.B.: Department of Biochemistry and Biophysics, Stockholm University, Svante Arrhenius väg 16, SE-106 91 Stockholm, Sweden.

Notes

The authors declare no competing financial interest.

■ ACKNOWLEDGMENTS

The authors acknowledge partial support from the French National Research Agency (ANR, NiFe-Cat project; Grant ANR-10-BLAN-711, and Labex program ARCANE; Grant ANR-11-LABX-0003-01), the COST Action CM1202 PERSPECT-H_2O, and the Life Science Division of the CEA (Irtelis and 2011 DSV-Energy programs). G.B. gratefully acknowledges support from Bengt Lundqvist minnesfond, FORMAS (Contract 213-2010-563), and the Swedish Royal Academy of Sciences. Work at the Argonne National Laboratory was supported by funding from the Division of Chemical Sciences, Biosciences, Office of Basic Energy Sciences of the U.S. Department of Energy through Grant DE-AC02-06CH11357. The authors thank Sunshine Silver (Argonne National Laboratory) for ICP-AES measurements.

■ REFERENCES

(1) Armstrong, F. A.; Hirst, J. *Proc. Natl. Acad. Sci. U.S.A.* **2011**, *108*, 14049−14054.
(2) Madden, C.; Vaughn, M. D.; Diez-Perez, I.; Brown, K. A.; King, P. W.; Gust, D.; Moore, A. L.; Moore, T. A. *J. Am. Chem. Soc.* **2012**, *134*, 1577−1582.
(3) Jones, A. K.; Sillery, E.; Albracht, S. P. J.; Armstrong, F. A. *Chem. Commun.* **2002**, 866−867.
(4) Canaguier, S.; Artero, V.; Fontecave, M. *Dalton Trans.* **2008**, 315−325.
(5) Tard, C.; Pickett, C. J. *Chem. Rev.* **2009**, *109*, 2245−2274.
(6) Simmons, T. R.; Berggren, G.; Bacchi, M.; Fontecave, M.; Artero, V. *Coord. Chem. Rev.* **2014**, *270−271*, 127−150.
(7) Chenevier, P.; Mugherli, L.; Darbe, S.; Darchy, L.; DiManno, S.; Tran, P. D.; Valentino, F.; Iannello, M.; Volbeda, A.; Cavazza, C.; Artero, V. *C. R. Chim.* **2013**, *16*, 491−516.
(8) Fontecave, M.; Artero, V. *C. R. Chim.* **2011**, *14*, 362−371.
(9) DuBois, M. R.; DuBois, D. L. *Chem. Soc. Rev.* **2009**, *38*, 62−72.
(10) Artero, V.; Chavarot-Kerlidou, M.; Fontecave, M. *Angew. Chem., Int. Ed.* **2011**, *50*, 7238−7266.
(11) Baffert, C.; Artero, V.; Fontecave, M. *Inorg. Chem.* **2007**, *46*, 1817−1824.
(12) Razavet, M.; Artero, V.; Fontecave, M. *Inorg. Chem.* **2005**, *44*, 4786−4795.
(13) Hu, X.; Brunschwig, B. S.; Peters, J. C. *J. Am. Chem. Soc.* **2007**, *129*, 8988−8998.
(14) Hu, X. L.; Cossairt, B. M.; Brunschwig, B. S.; Lewis, N. S.; Peters, J. C. *Chem. Commun.* **2005**, 4723−4725.
(15) Fourmond, V.; Jacques, P. A.; Fontecave, M.; Artero, V. *Inorg. Chem.* **2010**, *49*, 10338−10347.
(16) Jacques, P.-A.; Artero, V.; Pécaut, J.; Fontecave, M. *Proc. Natl. Acad. Sci. U.S.A.* **2009**, *106*, 20627−20632.
(17) Bhattacharjee, A.; Andreiadis, E. S.; Chavarot-Kerlidou, M.; Fontecave, M.; Field, M. J.; Artero, V. *Chem.—Eur. J.* **2013**, *19*, 15166−15174.
(18) McCrory, C. C. L.; Uyeda, C.; Peters, J. C. *J. Am. Chem. Soc.* **2012**, *134*, 3164−3170.
(19) Connolly, P.; Espenson, J. H. *Inorg. Chem.* **1986**, *25*, 2684−2688.
(20) Szajna-Fuller, E.; Bakac, A. *Eur. J. Inorg. Chem.* **2010**, 2488−2494.

(21) Andreiadis, E. S.; Jacques, P.-A.; Tran, P. D.; Leyris, A.; Chavarot-Kerlidou, M.; Jousselme, B.; Matheron, M.; Pécaut, J.; Palacin, S.; Fontecave, M.; Artero, V. *Nat. Chem.* **2013**, *5*, 48−53.
(22) Probst, B.; Guttentag, M.; Rodenberg, A.; Hamm, P.; Alberto, R. *Inorg. Chem.* **2011**, *50*, 3404−3412.
(23) Guttentag, M.; Rodenberg, A.; Kopelent, R.; Probst, B.; Buchwalder, C.; Brandstatter, M.; Hamm, P.; Alberto, R. *Eur. J. Inorg. Chem.* **2012**, 59−64.
(24) Wakerley, D. W.; Reisner, E. *Phys. Chem. Chem. Phys.* **2014**, *16*, 5739−5746.
(25) Cobo, S.; Heidkamp, J.; Jacques, P.-A.; Fize, J.; Fourmond, V.; Guetaz, L.; Jousselme, B.; Ivanova, V.; Dau, H.; Palacin, S.; Fontecave, M.; Artero, V. *Nat. Mater.* **2012**, *11*, 802−807.
(26) Lu, Y. *Angew. Chem., Int. Ed.* **2006**, *45*, 5588−601.
(27) Deuss, P. J.; den Heeten, R.; Laan, W.; Kamer, P. C. J. *Chem.—Eur. J.* **2011**, *17*, 4680−4698.
(28) Heinisch, T.; Ward, T. R. *Curr. Opin. Chem. Biol.* **2010**, *14*, 184−199.
(29) Faiella, M.; Roy, A.; Sommer, D.; Ghirlanda, G. *Biopolymers* **2013**, *100*, 558−571.
(30) Yu, F.; Cangelosi, V. M.; Zastrow, M. L.; Tegoni, M.; Plegaria, J. S.; Tebo, A. G.; Mocny, C. S.; Ruckthong, L.; Qayyum, H.; Pecoraro, V. L. *Chem. Rev.* **2014**, *114*, 3495−3578.
(31) Utschig, L. M.; Silver, S. C.; Mulfort, K. L.; Tiede, D. M. *J. Am. Chem. Soc.* **2011**, *133*, 16334−16337.
(32) Ueno, T.; Ohashi, M.; Kono, M.; Kondo, K.; Suzuki, A.; Yamane, T.; Watanabe, Y. *Inorg. Chem.* **2004**, *43*, 2852−2858.
(33) Ohashi, M.; Koshiyama, T.; Ueno, T.; Yanase, M.; Fujii, H.; Watanabe, Y. *Angew. Chem., Int. Ed.* **2003**, *42*, 1005−1008.
(34) Ueno, T.; Abe, S.; Yokoi, N.; Watanabe, Y. *Coord. Chem. Rev.* **2007**, *251*, 2717−2731.
(35) Carey, J. R.; Ma, S. K.; Pfister, T. D.; Garner, D. K.; Kim, H. K.; Abramite, J. A.; Wang, Z. L.; Guo, Z. J.; Lu, Y. *J. Am. Chem. Soc.* **2004**, *126*, 10812−10813.
(36) Abe, S.; Ueno, T.; Reddy, P. A. N.; Okazaki, S.; Hikage, T.; Suzuki, A.; Yamane, T.; Nakajima, H.; Watanabe, Y. *Inorg. Chem.* **2007**, *46*, 5137−5139.
(37) Ueno, T.; Koshiyama, T.; Abe, S.; Yokoi, N.; Ohashi, M.; Nakajima, H.; Watanabe, Y. *J. Organomet. Chem.* **2007**, *692*, 142−147.
(38) Utschig, L. M.; Tiede, D. M.; Poluektov, O. G. *Biochemistry* **2010**, *49*, 9682−9684.
(39) Bakac, A.; Espenson, J. H. *J. Am. Chem. Soc.* **1984**, *106*, 5197−5202.
(40) Broomhead, J. A.; Young, C. G. *Inorg. Synth.* **1982**, *21*, 127−128.
(41) Janda, M.; Hemmerich, P. *Angew. Chem., Int. Ed. Engl.* **1976**, *15*, 443−444.
(42) Weisbuch, S.; Gerard, F.; Pasdeloup, M.; Cappadoro, J.; Dupont, Y.; Jamin, M. *Biochemistry* **2005**, *44*, 7013−7023.
(43) Elliott, J. I.; Brewer, J. M. *Arch. Biochem. Biophys.* **1978**, *190*, 351−357.
(44) Poluektov, O. G.; Utschig, L. M.; Schlesselman, S. L.; Lakshimi, K. V.; Brudvig, G. W.; Kothe, G.; Thurnauer, M. C. *J. Phys. Chem. B* **2002**, *106*, 8911−8916.
(45) Stoll, S.; Schweiger, A. *J. Magn. Reson.* **2006**, *178*, 42−55.
(46) O'Reilly, J. E. *Biochim. Biophys. Acta* **1973**, *292*, 509−515.
(47) Becke, A. D. *Phys. Rev. A* **1988**, *38*, 3098−3100.
(48) Becke, A. D. *J. Chem. Phys.* **1993**, *98*, 5648−5652.
(49) Stephens, P. J.; Devlin, F. J.; Chabalowski, C. F.; Frisch, M. J. *J. Phys. Chem.* **1994**, *98*, 11623−11627.
(50) Weigend, F.; Ahlrichs, R. *Phys. Chem. Chem. Phys.* **2005**, *7*, 3297−3305.
(51) Neese, F. *Wiley Interdiscip. Rev.: Comput. Mol. Sci.* **2011**.
(52) Klamt, A.; Schuurmann, G. *J. Chem. Soc., Perkin Trans. 2* **1993**, 799−805.
(53) Sinnecker, S.; Rajendran, A.; Klamt, A.; Diedenhofen, M.; Neese, F. *J. Phys. Chem. A* **2006**, *110*, 2235−2245.
(54) Field, M. J. *J. Chem. Theory Comput.* **2008**, *4*, 1151−1161.
(55) Li, H.; Robertson, A. D.; Jensen, J. H. *Proteins: Struct., Funct., Bioinf.* **2005**, *61*, 704−721.
(56) Jorgensen, W. L.; Maxwell, D. S.; Tirado Rives, J. *J. Am. Chem. Soc.* **1996**, *118*, 11225−11236.
(57) Stewart, J. J. P. *J. Mol. Model.* **2007**, *13*, 1173−1213.
(58) Tiede, D. M.; Mulfort, K. L.; Scott, A. M.; Bender, S. L.; Poluektov, O. G.; Utschig, L. M.; Chen, L. X.; Mardis, K. L. *Abstr. Pap. Am. Chem. Soc.* **2010**, *240*.
(59) Eliezer, D.; Yao, J.; Dyson, H. J.; Wright, P. E. *Nat. Struct. Biol.* **1998**, *5*, 148−155.
(60) Hargrove, M. S.; Barrick, D.; Olson, J. S. *Biochemistry* **1996**, *35*, 11293−11299.
(61) Niklas, J.; Mardis, K. L.; Rakhimov, R. R.; Mulfort, K. L.; Tiede, D. M.; Poluektov, O. G. *J. Phys. Chem. B* **2012**, *116*, 2943−2957.
(62) Bakac, A.; Brynildson, M. E.; Espenson, J. H. *Inorg. Chem.* **1986**, *25*, 4108−4114.
(63) Rockenbauer, A.; Budozahonyi, E.; Simandi, L. I. *Dalton Trans.* **1975**, 1729−1737.
(64) Wirt, M. D.; Bender, C. J.; Peisach, J. *Inorg. Chem.* **1995**, *34*, 1663−1667.
(65) Schrauzer, G. N.; Lee, L. P. *J. Am. Chem. Soc.* **1970**, *92*, 1551−1557.
(66) Jones, R. D.; Summerville, D. A.; Basolo, F. *Chem. Rev.* **1979**, *79*, 139−179.
(67) Westre, T. E.; Kennepohl, P.; DeWitt, J. G.; Hedman, B.; Hodgson, K. O.; Solomon, E. I. *J. Am. Chem. Soc.* **1997**, *119*, 6297−6314.
(68) It should be noted that the distance scale obtained from Fourier transform of the EXAFS data and displayed by Figure 8 is 0.5 Å lower than the real geometric distance between the cobalt center and its neighbors.
(69) Megnamisibelombe, M.; Nlend, G. N.; Nuber, B. *Bull. Chem. Soc. Jpn.* **1992**, *65*, 612−614.
(70) Sun, W.; Li, X. Q.; Wang, Y.; Li, X.; Zhao, C. Z.; Jiao, K. *Bioelectrochemistry* **2009**, *75*, 170−175.
(71) Zhao, G. C.; Zhang, L.; Wei, X. W.; Yang, Z. S. *Electrochem. Commun.* **2003**, *5*, 825−829.
(72) No signal is observed if complex **1** alone is deposited onto the MWCNTs and coated with Nafion under otherwise similar conditions.
(73) The absence of such a cobalt(III)/cobalt(II) signal in the cyclic voltammogram of the biohybrid species suggests that the formation of the EPR-silent cobalt(III) species discussed above does not simply rely on a monoelectronic process from the cobalt(II) species. This also provides a basis for explaining why it is not possible to convert this EPR-silent cobalt(III) state into the cobalt(II) state by incubating the sample with mild reductants such as sodium dithionite.
(74) Hemmerich, P.; Massey, V.; Fenner, H. *FEBS Lett.* **1977**, *84*, 5−21.
(75) Massey, V.; Hemmerich, P. *Biochemistry* **1978**, *17*, 9−16.
(76) Blankenhorn, G. *Eur. J. Biochem.* **1976**, *67*, 67−80.
(77) Duchstein, H. J.; Fenner, H.; Hemmerich, P.; Knappe, W. R. *Eur. J. Biochem.* **1979**, *95*, 167−181.
(78) Bhattacharjee, A.; Chavarot-Kerlidou, M.; Andreiadis, E. S.; Fontecave, M.; Field, M. J.; Artero, V. *Inorg. Chem.* **2012**, *51*, 7087−7093.
(79) Mulfort, K. L.; Tiede, D. M. *J. Phys. Chem. B* **2010**, *114*, 14572−14581.
(80) Vincent, K. A.; Tilley, G. J.; Quammie, N. C.; Streeter, I.; Burgess, B. K.; Cheesman, M. R.; Armstrong, F. A. *Chem. Commun.* **2003**, 2590−2591.
(81) Kleingardner, J. G.; Kandemir, B.; Bren, K. L. *J. Am. Chem. Soc.* **2013**, *136*, 4−7.
(82) Jones, A. K.; Lichtenstein, B. R.; Dutta, A.; Gordon, G.; Dutton, P. L. *J. Am. Chem. Soc.* **2007**, *129*, 14844−14845.
(83) Roy, A.; Madden, C.; Ghirlanda, G. *Chem. Commun.* **2012**, *48*, 9816−9818.
(84) Roy, S.; Shinde, S.; Hamilton, G. A.; Hartnett, H. E.; Jones, A. K. *Eur. J. Inorg. Chem.* **2011**, 1050−1055.
(85) Sano, Y.; Onoda, A.; Hayashi, T. *Chem. Commun.* **2011**, *47*, 8229−8231.

(86) Sano, Y.; Onoda, A.; Hayashi, T. *J. Inorg. Biochem.* **2012**, *108*, 159−162.
(87) The use of more acidic conditions (pH 4.5−4.7) allows one to observe higher turnover numbers of ∼80 within ∼2 h: Roy, A.; Madden, C.; Ghirlanda, G. *Chem. Commun.* **2012**, *48*, 9816−9818. Sano, Y.; Onoda, A.; Hayashi, T. *Chem. Commun.* **2011**, *47*, 8229−8231.
(88) Muckerman, J. T.; Fujita, E. *Chem. Commun.* **2011**, *47*, 12456−12458.
(89) Solis, B. H.; Hammes-Schiffer, S. *Inorg. Chem.* **2011**, *50*, 11252−11262.
(90) Dempsey, J. L.; Winkler, J. R.; Gray, H. B. *J. Am. Chem. Soc.* **2010**, *132*, 16774−16776.
(91) Simandi, L. I.; Szeverenyi, Z.; Budozahonyi, E. *Inorg. Nucl. Chem. Lett.* **1975**, *11*, 773−777.
(92) Silver, S. C.; Niklas, J.; Du, P. W.; Poluektov, O. G.; Tiede, D. M.; Utschig, L. M. *J. Am. Chem. Soc.* **2013**, *135*, 13246−13249.
(93) Letondor, C.; Pordea, A.; Humbert, N.; Ivanova, A.; Mazurek, S.; Novic, M.; Ward, T. R. *J. Am. Chem. Soc.* **2006**, *128*, 8320−8328.
(94) Pordea, A.; Creus, M.; Letondor, C.; Ivanova, A.; Ward, T. R. *Inorg. Chim. Acta* **2010**, *363*, 601−604.
(95) Ueno, T.; Koshiyama, T.; Ohashi, M.; Kondo, K.; Kono, M.; Suzuki, A.; Yamane, T.; Watanabe, Y. *J. Am. Chem. Soc.* **2005**, *127*, 6556−6562.